Journal of Nuclear Materials 618 (2026) 156171

Contents lists available at ScienceDirect

Journal of Nuclear Materials

journal homepage: www.elsevier.com/locate/jnucmat

# Synergistic effects of hydrogen and helium on He bubble evolution in bcc-iron: A kinetic model

Lihao Shi [a], Cianna Chen [a,b], Qing Peng [c,d,**], Fei Gao [a,e,*]

[a] Department of Nuclear Engineering and Radiological Sciences, University of Michigan, Ann Arbor, MI 48109, USA
[b] Pioneer High School, Ann Arbor, MI 48103, USA
[c] School of Power and Mechanical Engineering, Wuhan University, Wuhan 430072, China
[d] Xinyan Semi Technology Co. Ltd, Wuhan 430075, China
[e] Department of Materials Science and Engineering, University of Michigan, Ann Arbor, MI 48109, USA

## GRAPHICAL ABSTRACT

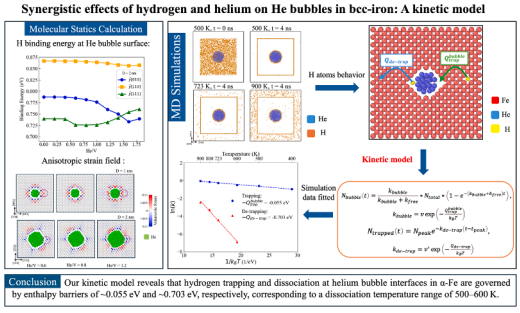


## ARTICLE INFO

*Keywords:*
He bubbles
Hydrogen
Molecular dynamics
Kinetic model
Trapping–detrapping enthalpies
Dissociation temperature

## ABSTRACT

Understanding how hydrogen interstitials interact with helium bubbles in iron-based materials is crucial for predicting and mitigating tritium retention and safety issues in fusion reactor components. In this work, a new kinetic model is developed to quantify hydrogen trapping and de-trapping enthalpies at helium bubble surfaces in $\alpha$-Fe, based on insights obtained from molecular dynamics simulations. We begin by assessing the influence of anisotropic stress fields—induced by He bubbles of varying sizes and helium densities—on hydrogen binding behavior using molecular statics. Our calculations reveal that high He densities shift the most favorable H binding sites, while smaller bubbles lead to reduced binding energies due to increased surface tension. Molecular dynamics simulations over a broad temperature range (400–900 K) are then used to track hydrogen trapping and de-trapping dynamics at bubble interfaces. The kinetic model captures these processes quantitatively, showing that hydrogen trapping is governed by an enthalpy barrier of ~0.055 eV, while a dissociation enthalpy of ~0.703 eV dictates hydrogen release, corresponding to a dissociation temperature range of 500–600 K. Additionally, we observe the formation of $H_2$ molecules near the bubble surface, with an associated activation barrier of ~0.90 eV. These results highlight the critical role of local stress fields in mediating hydrogen retention and release and

* Corresponding author at: Department of Nuclear Engineering and Radiological Sciences, University of Michigan, Ann Arbor, MI 48109, USA.
** Corresponding author at: School of Power and Mechanical Engineering, Wuhan University, Wuhan 430072, China.
*E-mail addresses:* pengqing@imech.ac.cn (Q. Peng), gaofeium@umich.edu (F. Gao).

https://doi.org/10.1016/j.jnucmat.2025.156171
Received 1 May 2025; Received in revised form 16 September 2025; Accepted 19 September 2025
Available online 20 September 2025

demonstrate the value of kinetic modeling in capturing the complex interplay between hydrogen and helium in fusion-relevant materials.

## 1. Introduction

In a deuterium–tritium fusion environment, 14 MeV neutrons induce atomic displacements and nuclear reactions, leading to the production of hydrogen and helium. These gases, known for their low solubility in iron-based alloys, tend to form bubbles or cavities, resulting in material swelling and embrittlement. Furthermore, the simultaneous accumulation of H and He intensifies microstructural damage through a synergistic effect, accelerating material degradation and presenting significant challenges in the design of fusion reactor components [1].

Early studies underscored the role of inert gases, particularly helium, in cavity nucleation and growth [2,3], a process further elucidated by Zhang et al. [4] and Han et al. [5], who highlighted helium's essential role in cavity nucleation and the efficiency of grain boundaries as sinks for irradiation-induced vacancies. Atomistic simulations reveal that helium bubble growth at Σ3 and Σ73b grain boundaries in BCC iron involves dislocation loop emission, self-interstitial accumulation, and structural reconstruction, with bubble morphology and defect evolution strongly influenced by local helium concentration and grain boundary character [6,7]. The simultaneous presence of hydrogen introduces additional complexities, as it interacts with helium bubbles to further alter the microstructural evolution under irradiation. Farrell and Lee [8] examined ion-induced damage in Fe-10Cr-6Mo-0.5Nb ferritic steel under heavy-ion irradiation, revealing that co-implantation of 500 appm helium and 100 appm deuterium increases cavity density by over 50 %, expands cavitation to higher temperatures. The co-implantation significantly alters cavity size distribution, amplifying irradiation-induced damage. Triple ion beam irradiation ($Fe^{3+}$, $He^{+}$ and $H^{+}$) on F82H ferritic/martensitic steel shows that at 470 °C, swelling under triple beams reached 3.2 %, compared to only 0.08 % under dual beams, highlighting the profound impact of hydrogen on cavity formation and swelling [9]. In Fe–Cr ferritic model alloys, single, dual, and triple ion-beam irradiation experiments at temperatures between 470 °C and 600 °C revealed that while helium significantly enhanced cavity nucleation and swelling (up to 0.4 % under dual ion irradiation), the presence of hydrogen alone had minimal effects. However, under triple ion irradiation, the combined effect of helium and hydrogen led to larger cavities and significantly increased swelling, up to 4 % [10]. Dual irradiation ($He^{+}$ and $H^{+}$) on Reduced-activation ferritic/martensitic (RAFM) steels showed that hydrogen enhances helium bubble nucleation and growth, with peak swelling rates observed at 450 °C, while higher temperatures led to reduced swelling due to increased mobility and annihilation of defects [11].

Recent studies by Clowers et al. [12] revealed the spatial distribution of hydrogen within the irradiated microstructure of triple-ion-irradiated $Fe_8Cr_2W$ at 450 °C, forming a shell-like structure of hydrogen surrounding the cavity, while helium predominantly resides at the cavity's center. This hydrogen halo structure has also been observed by Judge et al. [13] and Zimber et al. [14] in their investigations of hydrogen-helium interactions within helium bubbles in irradiated X-750 Ni-based alloys and Eurofer-97 RAFM steel, respectively. However, the stability of hydrogen trapped at helium-filled cavity surfaces under experimental temperatures remains unexplored despite its importance.

Density functional theory (DFT) calculations have demonstrated that vacancies serve as the strongest traps for hydrogen, with a binding energy of approximately 0.57 eV [15]. Hydrogen-monovacancy complexes ($VH_2$) exhibit significant negative heat of solution for hydrogen, with a formation energy of 0.60 eV. However, limited information is available on the interactions of H with vacancy defects containing He atoms [16]. Notably, the research by Hayward et al. [17] demonstrated a synergetic effect between H and He in bubbles, enhancing bubble growth through H-aided loop punching. Their calculations revealed a core-shell structure within helium bubbles, with helium atoms at the core and hydrogen atoms forming a surrounding shell. The DFT studies [18] indicated that the binding energy of hydrogen to a defect cluster $V_1He_1$ is notably weaker, ranging between 0.2 and 0.4 eV. At a bcc Fe-He interface [19], hydrogen binding energy is highest under vacuum conditions, reaching values of 0.59 eV, 0.92 eV, and 0.76 eV for (100), (110), and (111) surfaces, respectively, and decreases with increasing helium density. These binding energies are insufficient to stabilize H atoms at cavity surfaces during high-temperature irradiation (e.g., 450 °C or above). Molecular dynamic (MD) simulation was applied to explored He bubble (void) trapping capacity for H of different temperature and He density. The H de-trapping temperature is estimated to be 310 K [20] and the formation of $H_2$ molecular was observed. However, the interatomic potential for H-H interactions in previous MD simulations was unnaturally strong and attractive, contradicting DFT results [21]. Wu et al. [22] employed a newly developed DP-FeHHe potential to simulate hydrogen behavior near helium-vacancy clusters at 300 K for 4 ns, observing hydrogen aggregation around the cluster surface. Despite significant progress in understanding hydrogen behavior near helium bubbles, computational simulations often fail to reproduce experimental observations, underscoring key gaps in our understanding.

Our objective is to investigate the mechanisms of which hydrogen atoms diffuse in Fe, interact with and subsequently retain on the He bubble surfaces. Here we describe the results of comprehensive molecular statics (MS) calculations to investigate the anisotropic strain-stress fields induced by helium bubbles with different sizes and helium densities, as well as their influence on hydrogen binding energies across different crystallographic orientations. Meanwhile, MD simulations are utilized to examine the temperature-dependent dynamics of hydrogen trapping and de-trapping at helium bubble surfaces. A kinetic model is introduced to quantitatively determine activation barriers of hydrogen trapping and de-trapping and to evaluate the complex interplay between helium density, bubble dimensions, and the resultant local stress fields.

## 2. Method

### 2.1. Molecular statics calculations

Molecular statics calculations and molecular dynamics simulations were performed using the Large-Scale Atomic/Molecular Massively Parallel Simulator (LAMMPS) [23]. To accurately model the interactions in the Fe-He-H system, a combination of well-established potentials was employed. The Fe-He interaction was described using the s-band model potential developed by Gao et al. [24]. For Fe-Fe interactions, the Ackland-Mendelev potential [25] was utilized, while the He-He interaction was modeled with the Aziz potential (Hartree-Fock-dispersion potential) [26]. Additionally, to capture the behavior of hydrogen, including its interactions within the perfect BCC Fe lattice, its binding to lattice defects such as vacancies and surfaces, and H-H interactions in the Fe matrix, many-body potentials developed recently by Wen [27] were employed. This potential provides an accurate description of H-H interactions in the Fe lattice and effectively captures the $H_2$ formation process on the Fe surface, both in agreement with DFT results, with detailed calculations provided in Section 3.4. The weak van der Waals interactions between He and H were described by Lennard-Jones potential with parameters of $\sigma = 1.333\ \AA$ and $\varepsilon = 5.9225 \times 10^{-4}$ eV [28].

To investigate the effect of the anisotropic strain field generated by a helium bubble on the hydrogen binding energy, we constructed three distinct Fe supercells with the different crystallographic orientations of

the Fe matrix. The supercell $\hat{y}[010]$ had crystallographic axes aligned along [100], [010] and [001]. The supercell $\hat{y}[110]$ had oriented along $[1\bar{1}0]$, [110] and [001], while the supercell $\hat{y}[111]$ was defined by $[1\bar{1}0]$, [111] and $[\bar{1}\bar{1}2]$. In each case, hydrogen atoms were positioned along the $\hat{y}$-direction to evaluate the binding energy under the influence of anisotropic strain field. Fig. 1 presents a schematic representation of Fe-He supercells for three different cases, visualized using OVITO [29].

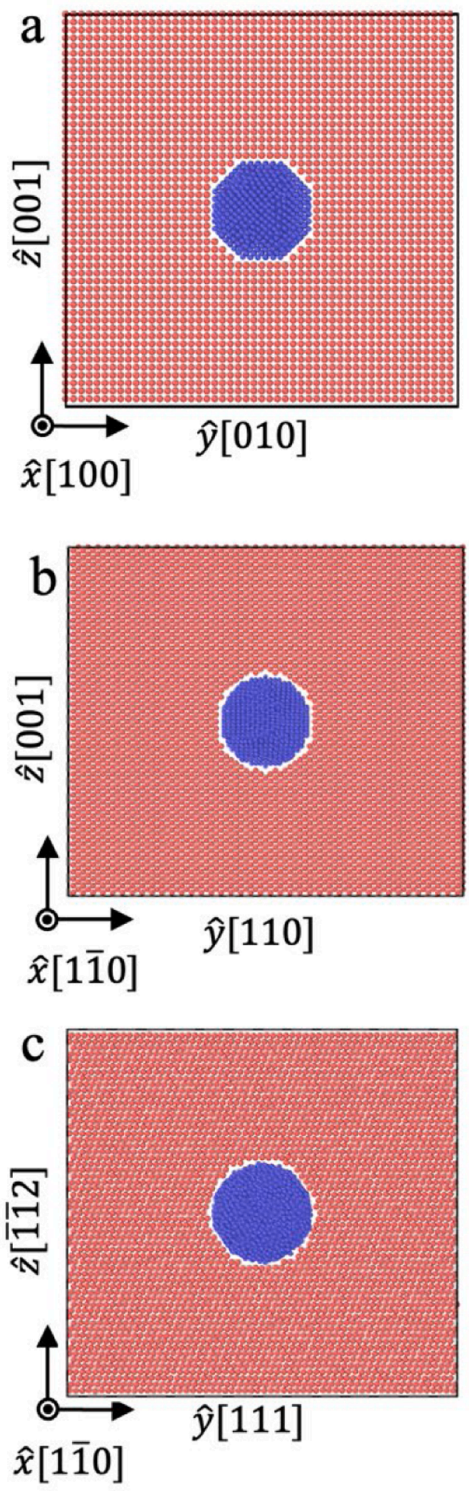


**Fig. 1.** Schematic of Fe supercells containing a helium bubble with a diameter of 4 nm at the center, oriented along three different crystallographic directions: (a) $\hat{y}[010]$; (b) $\hat{y}[110]$; (c) $\hat{y}[111]$. The red spheres represent Fe atoms, while the blue spheres represent, He atoms. The axes are labeled to indicate the orientations of the crystallographic directions in each configuration.

Periodic boundary conditions were applied in all three dimensions, and the supercell dimensions were chosen to prevent interactions between the helium cavity and its periodic images. For the $\hat{y}[010]$ supercell, the dimensions are $50a_0 \times 50a_0 \times 50a_0$, where $a_0$ is 2.855 Å, containing a total of 250,000 Fe atoms. For the $\hat{y}[110]$ supercell, the dimensions are $40a_0 \times 40a_0 \times 40a_0$ with a total of 320,000 Fe atoms and $\hat{y}[111]$ supercell has dimensions of $40a_0 \times 30a_0 \times 30a_0$ and contains 28,816 Fe atoms. A helium cavity was introduced by firstly creating a void at the center of the supercell, then randomly inserting helium atoms into this void. Three cavity sizes were examined, with diameters of 1 nm, 2 nm, and 4 nm. The helium density within each cavity was characterized by the ratio of helium atoms to vacancies (He/V), which was varied from 0 to 1.8. Given the liquid-like nature of helium inside bubbles in the Fe matrix, it is essential to ensure that the bubble reaches a relatively low-energy state before further calculations. To achieve this, each configuration underwent annealing at 300 K for 0.2 ns, followed by quenching to 0 K. This annealing–quenching cycle was repeated three times with different random number seeds, thereby generating three independent helium bubble configurations for each case. Subsequently, conjugate gradient (CG) minimization with energy and force tolerances of $10^{-20}$ eV/atom and $10^{-20}$ eV/Å, respectively, was performed to relax the supercell into a minimum-energy configuration. These multiple realizations were then used in subsequent calculations to obtain statistically reliable results.

For each independent He bubble configuration, a hydrogen interstitial was introduced either at the Fe–He interface or at a tetrahedral interstitial site in the bulk. The bulk site was placed at least 4 nm away from both the interface and the free surface to eliminate spurious boundary interactions. In each case, conjugate gradient (CG) minimization was performed with fixed supercell dimensions, allowing the atomic positions to relax, to obtain the total energy of the system. To assess the validity of this constant-volume approximation, we compared hydrogen binding energies obtained from constant-volume and variable-cell relaxations for a 2 nm helium bubble along the [010], [110], and [111] orientations. The results showed negligible differences for the MD block used, with deviations typically less than 0.01 eV (see Supplementary Fig. S1). Furthermore, binding energies reported in this work were averaged over three independent helium bubble configurations for each orientation, further reducing any residual bias from the constant-volume treatment. The binding energy of a hydrogen atom at the Fe-He interface, along the different surface orientations, is defined as:

$$E_{\mathrm{b},\,\hat{y}}^{\mathrm{interface}} = E_{\mathrm{total},\,\hat{y}}^{\mathrm{bulk}} - E_{\mathrm{total},\,\hat{y}}^{\mathrm{interface}}, \tag{2}$$

where, $E_{\mathrm{total},\,\hat{y}}^{\mathrm{interface}}$ is the total energy of the Fe-He supercell with a solute H atom at the interface, and $E_{\mathrm{total},\,\hat{y}}^{\mathrm{bulk}}$ is the total energy of the same supercell with a H atom at the tetrahedral interstitial site in the bulk.

Climbing-Image Nudged Elastic Band (CI-NEB) calculations [30,31] were performed to evaluate the impact of helium densities on the energy barrier for hydrogen migration from the Fe–He interface into the Fe bulk. Specifically, the migration barriers were calculated for hydrogen adsorbed at the Fe surface near the interface, as it migrates to an interstitial site within the Fe matrix.

### 2.2. Molecular dynamic simulation

MD simulations were performed to investigate how interstitial hydrogen in BCC Fe is captured by helium bubbles and subsequently released from their surfaces. A $50a_0 \times 50a_0 \times 50a_0$ supercell of BCC Fe was constructed along the [100], [010] and [001] directions. The simulated temperatures are 400 K, 500 K, 600 K, 723 K, 800 K, and 900 K, with the corresponding lattice parameters of 2.8625 Å, 2.8680 Å, 2.8720 Å, 2.8744 Å, and 2.8779 Å, respectively. A 5 nm void was introduced at

the center, created by removing Fe atoms to form the same-sized cavity across all the temperatures. To maintain the same physical bubble size across all temperatures, the number of removed atoms was slightly adjusted based on the lattice parameter: 5577 vacancies were created for simulations at 400 K and 500 K, and 5601 vacancies were used for temperatures from 600 K to 900 K. This fixed-size approach was adopted to isolate the effect of temperature on hydrogen behavior while minimizing the influence of changes in bubble curvature or surface area.

Helium atoms were randomly inserted into the void at He/V ratios of 0, 0.2, 0.5, and 1. Subsequently, an equal number of hydrogen atoms (H/V = 1) was introduced into the Fe matrix. A $10a_0$-thick vacuum layer was added on both sides of the supercell to allow hydrogen to evaporate into the vacuum.

To keep cell dimensions fixed during the dynamic simulations, the outermost layer of Fe atoms was immobilized by setting their forces and velocities to zero. Additionally, hydrogen molecules evaporating into the vacuum layer were also constrained. Energy minimization was conducted with the fixed supercell dimensions, using the same energy and force tolerances as in previous calculations. The system was then relaxed and simulated in the canonical (NVT) ensemble, where temperature control was maintained using a Nosé-Hoover thermostat [32,33], with a time step of 0.0001 ps for a total duration of 4 ns.

## 3. Results

### 3.1. Binding energies of a single hydrogen at the Fe-He interface

Hydrogen binding energies calculated as the total energy difference of the supercell with a H atom solute at Fe-He interface and at a stable position in the bulk. The tetrahedral interstitial site (TIS) is selected as the most stable position in the bulk, as calculated in previous DFT calculations [34].

In our molecular statics calculations, each hydrogen binding energy was averaged over three independently generated He bubble configurations to ensure statistically reliable results. Fig. 2 presents the hydrogen binding energy as a function of helium density (He/V ratio) for bubble diameters of 1 nm, 2 nm, and 4 nm, along three crystallographic orientations: $\hat{y}[010]$, $\hat{y}[110]$ and $\hat{y}[111]$. The maximum value of H binding energy is observed at $\hat{y}[110]$ direction in the voids across all cavity size, which aligns with the *ab-initio* calculations of H binding energy on a Fe(110) surface [19,35]. Error bars derived from the averaging process are included in Fig. 2, but they are very small (<0.005 eV) and barely visible, indicating that variations among different He bubble configurations contribute negligibly to the overall binding energy values. This further confirms the robustness of the statistical averaging procedure.

The variations in hydrogen binding energy with He/V ratio closely follow the changes in the local atomic strain field around the bubble

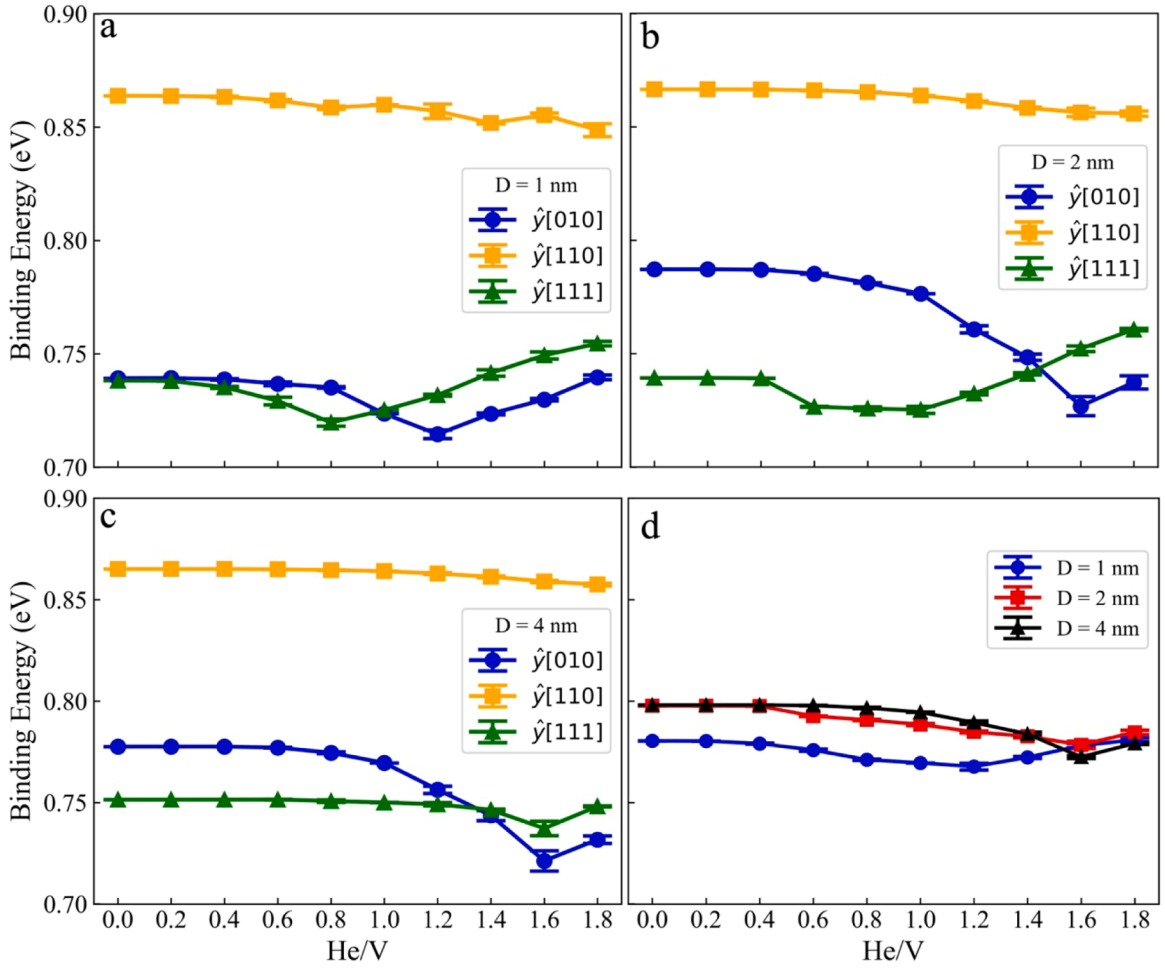


**Fig. 2.** (a–c) Hydrogen binding energies as a function of helium density (He/V ratio) for three bubble diameters (1 nm, 2 nm, and 4 nm) and orientations: $\hat{\boldsymbol{y}}[010]$, $\hat{\boldsymbol{y}}[110]$ and $\hat{\boldsymbol{y}}[111]$. Error bars indicate the statistical variation obtained by averaging over three independent He bubble configurations. (d) Orientation-averaged binding energies plotted as a function of the He/V ratio for helium bubbles of 1 nm, 2 nm, and 4 nm diameters. As the He/V ratio increases, the binding energies for all bubble sizes converge, suggesting that helium-induced stress fields within the bubble dominate over surface tension effects at higher helium densities.

surface. Tensile regions tend to stabilize hydrogen, resulting in higher binding energies, while compressive regions destabilize it and lowering the binding energies. Along $\hat{y}[010]$ direction, the local strain changes from slightly tensile (+0.0078 at He/V = 0.2) to significantly compressive (−0.024 at He/V = 1.6), accompanied by a decrease in binding energy from 0.787 eV to 0.733 eV. In contrast, along the $\hat{y}[111]$ direction, tensile strain dominates: the strain increases from +0.0033 to +0.0137 over the same He/V range, and the binding energy rises from 0.726 eV to 0.754 eV. This behavior is consistent with previous DFT studies [36], which have showed that tensile hydrostatic stress in bcc Fe increases the binding energy of interstitial hydrogen, whereas compressive stress reduces it.

Local stresses around the bubble also shift hydrogen's preferred binding site. In the $\hat{y}[010]$ orientation, the binding energy initially decreases with increasing helium density, reaching a minimum before rising again. At low He/V ratios, hydrogen is stabilized at hollow sites near the interface, as shown in Fig. 3(a). As the helium-induced compressive strain intensifies, the hollow site becomes less favorable, and hydrogen shifts to a quasi-threefold site [35], as shown in Fig. 3(b). In the $\hat{y}[111]$ orientation, the tensile strain field drives a different transition: hydrogen moves from a quasi-fourfold site [37], as shown in Fig. 3(c), to the site shown in Fig. 3(d). The volumetric strain distributions in Fig. 3, calculated using OVITO [29] with zero-K Fe–void configurations as the reference. Displacements of atoms from their reference positions were utilized to compute Green–Lagrangian strain tensors, ultimately yielding volumetric strain measurements [38,39]. The increasing He/V ratio amplifies compressive strain along the $\hat{y}[010]$ direction and tensile strain in the $\hat{y}[111]$ direction, underscoring the anisotropic nature of the helium-induced strain field.

The average binding energy of three crystallographic orientations is calculated by: $E^{\text{ave}}_{\text{b},\ \hat{y}} = \frac{1}{3}\left(E^{\text{interface}}_{\text{b},\ \hat{y}[010]} + E^{\text{interface}}_{\text{b},\ \hat{y}[110]} + E^{\text{interface}}_{\text{b},\ \hat{y}[111]}\right)$, as shown in Fig. 2(d). At lower He/V ratios, the smaller bubbles with a diameter of 1 nm exhibit slightly lower binding energies compared to the larger bubbles with the diameters of 2 nm and 4 nm. This difference can be attributed to the higher surface tension of the smaller bubbles, which amplifies the localized stress fields and influences the stability of hydrogen binding positions. As the He/V ratio increases, however, the binding energies for all bubble sizes converge. This suggests that the stress fields generated by helium atoms within the bubble dominate over the effects of surface tension, making bubble size have a negligible impact on hydrogen binding energy at higher helium densities.

### 3.2. Hydrogen migration energy barrier at the Fe-He interface to Fe bulk

The He density plays a significant role in influencing the H migration energy barrier into the Fe (100) surface. Fig. 4(a) presents the CI-NEB energy calculations for a hydrogen atom migrating from the Fe–He interface into the Fe bulk along the $\hat{y}[010]$ direction for three helium densities (He/V = 0, 0.6, and 1.2) in a 2 nm bubble system. For the low and moderate helium densities of He/V = 0 and 0.6, the first local minimum appears at approximately 2.72 Å from the trapped site (reaction coordinate 0), a stable position close to the interface. By contrast, when He/V = 1.2, this local minimum effectively disappears, and the hydrogen atom migrates farther to a new stable position at around 3.68 Å. This shift can be attributed to the compressive stress imposed by the high helium concentration, which alters the potential energy landscape near the interface. Furthermore, the highest He density, 1.2 He/V, smooths the migration barrier over a range extending to approximately 5.7 Å, diminishing or merging the intermediate peaks observed at lower He densities. This trend aligns with ab-initio calculations reported in ref [19], where at He/V ratio of 2, several barriers are completely removed, and the energy barriers generally flatten up to 5.12 Å below the Fe (100) surface. These results indicate that increasing helium content not only destabilizes the first hydrogen trapping site near the interface but also flattens the energy barriers along the migration path into the bulk.

The migration of hydrogen into the Fe surface along the $\hat{y}[111]$ orientation (as shown in Fig. 4 b) exhibits minimal dependence on the helium density. At a He/V ratio of 0.6, the migration barriers remain nearly unchanged compared to a vacuum surface case. However, at a He/V ratio of 1.2, hydrogen migration begins with diffusion to another

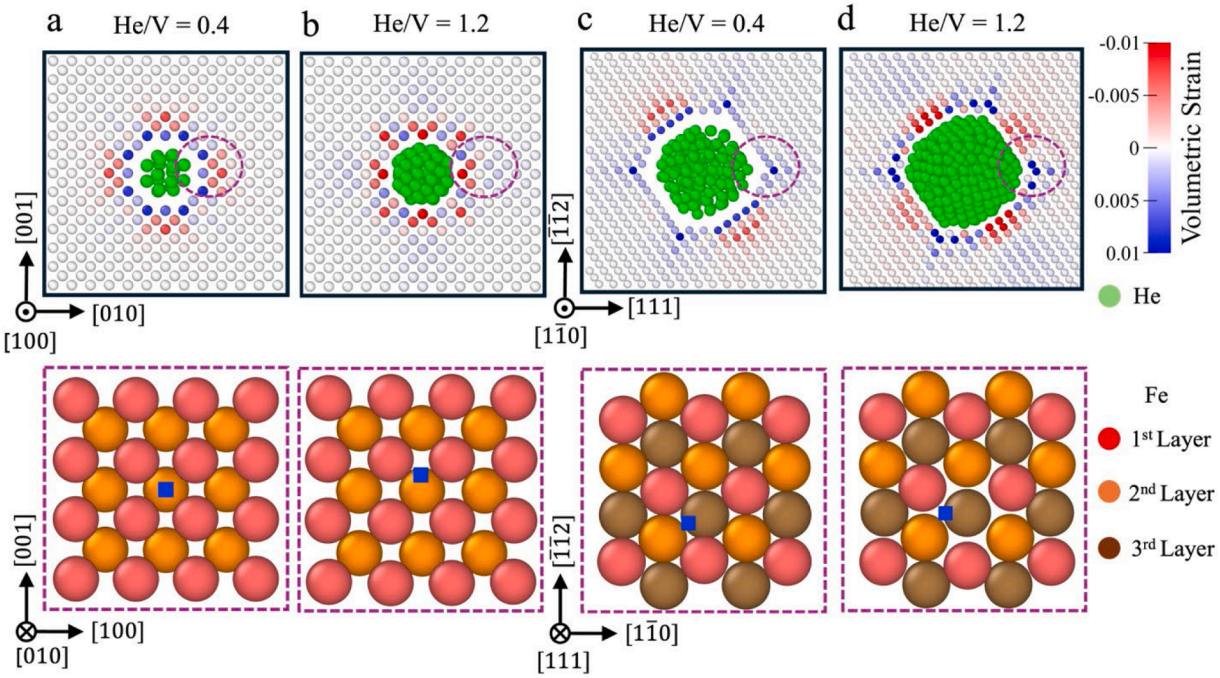


**Fig. 3.** Volumetric strain fields (top row) and corresponding hydrogen preferred binding sites (bottom row) for helium bubbles in bcc Fe. (a–b) 1 nm diameter bubbles with He/V = 0.4 and 1.2 along the $\hat{y}[010]$ orientation; (c–d) 2 nm diameter bubbles with He/V = 0.4 and 1.2 along the $\hat{y}[111]$ orientation. Green spheres denote helium atoms, while red, orange, and brown spheres represent the first, second, and third Fe atomic layers adjacent to the bubble interface. Purple circles in the top row indicate the regions where hydrogen binding sites are located, which are shown with bule square.

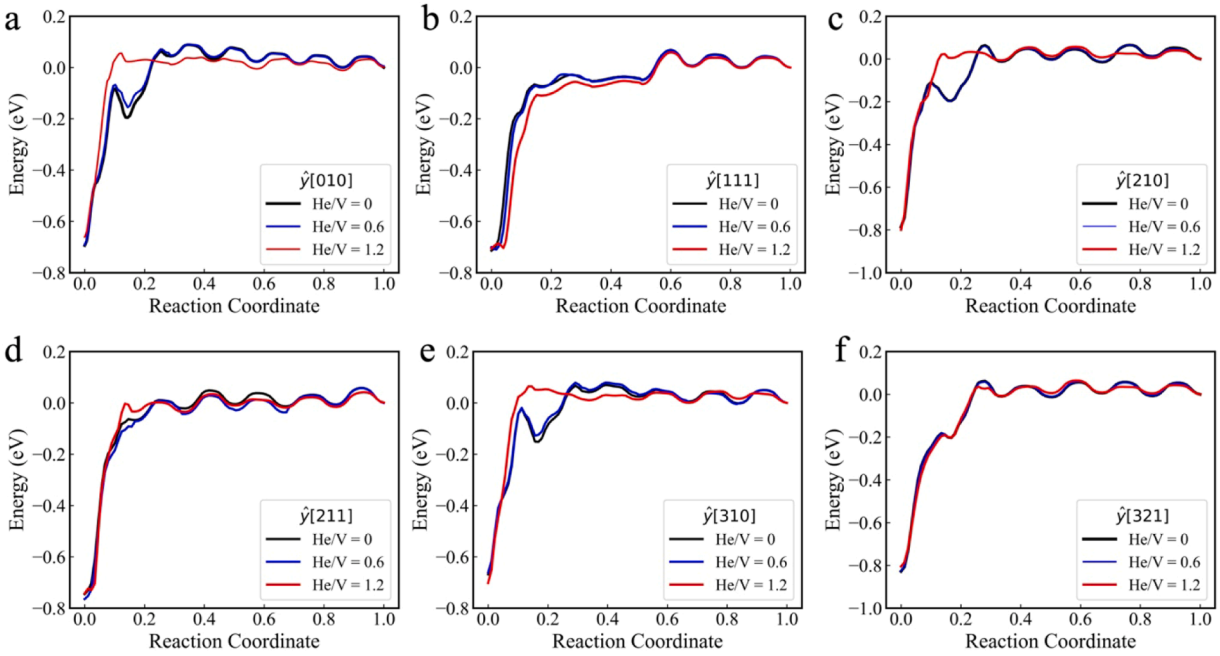


**Fig. 4.** CI-NEB energy profiles for hydrogen migration from the Fe–He interface into the Fe bulk along six crystallographic directions: (a) $\hat{\boldsymbol{y}}$[010], (b) $\hat{\boldsymbol{y}}$[111], (c) $\hat{\boldsymbol{y}}$[210], (d) $\hat{\boldsymbol{y}}$[211], (e) $\hat{\boldsymbol{y}}$[310], and (f) $\hat{\boldsymbol{y}}$[321], in a 2 nm helium bubble system with He/V = 0, 0.6, and 1.2. The [010], [210], [211], and [310] directions show that increasing helium density suppresses the first near-interface minimum and lowers the overall barrier, whereas the [111] and [321] directions remain largely unaffected by helium density.The reaction coordinate starts at 0, representing the Fe–He interface, and ends at the interstitial site in the Fe bulk.

surface site, introducing a negligible energy barrier. This is the primary difference compared to the void and He/V = 0.6 cases, slightly reducing the initial migration energy of hydrogen into the Fe surface.

To further assess directional dependence, migration paths along high-index orientations [210], [211], [310], and [321] were also examined. The [210], [211], and [310] directions exhibit behavior consistent with [010]: in these cases, increasing helium density suppresses the first near-interface minimum and lowers the barrier height. In contrast, the [321] path, in contrast, resembles the [111] case, showing only weak sensitivity to helium density.

Overall, these additional migration paths reinforce the observation that helium density primarily destabilizes the first hydrogen trapping site and flattens the migration barrier along directions normal or near-normal to the (100) surface, whereas more oblique directions such as [111] and [321] remain largely unaffected.

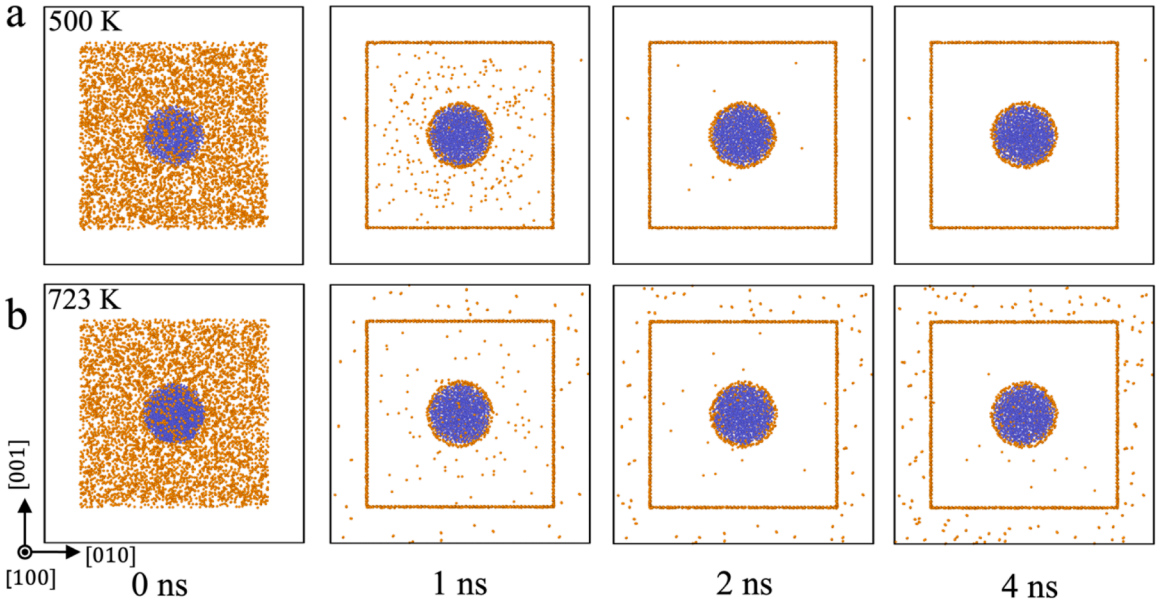


**Fig. 5.** Molecular dynamics simulation snapshots of hydrogen migration and interaction with a helium bubble (He/V = 0.5) in BCC Fe bulk at (a) 500 K and (b) 723 K. A $10\boldsymbol{a}_0$-thick vacuum layer is introduced to allow hydrogen atoms to escape. Orange spheres represent hydrogen atoms, blue spheres represent helium atoms, and Fe atoms are omitted for clarity. At 500 K, hydrogen atoms either migrate to the free surface or are captured by the helium bubble after 4 ns. At 723 K, hydrogen atoms initially captured by the helium bubble exhibit de-trapping behavior, re-entering the Fe bulk. The formation and subsequent evaporation of hydrogen molecules into the vacuum are visible in the depicted vacuum regions.

### 3.3. MD simulation of H atoms captured by He bubbles

For temperature-dependent studies, He/V=0.5 was selected as a representative case. Under applied thermal conditions, hydrogen atoms initially occupying interstitial sites diffuse throughout the material, eventually migrating to sinks such as the He bubble surface and the free surface. This dynamic behavior is governed by the temperature-driven mobility of H atoms and the trapping potential of these sinks.

At the temperatures below 500 K, the dominant process observed is the accumulation of H atoms on the bubble and free surfaces, where they become trapped. Over time, a stable layer of H atoms forms on the bubble surface. However, as the temperature increases beyond 500 K, an additional mechanism, namely de-trapping, becomes evident. In this process, H atoms, once bound to the bubble surface, gain sufficient energy to overcome the trapping potential, leading to their dissociation and reenter into the bulk matrix. Higher temperatures further enhance de-trapping, as the thermal energy available to H atoms increases, reducing the stability of the trapped state.

As shown in Fig. 5, the time evolution of trapped hydrogen atoms illustrates the critical role of both time and temperature in governing the dynamics of hydrogen trapping and de-trapping at helium bubble sink. The transition between trapping-dominated and trapping-de-trapping dynamics provides key insights into the thermal stability and mobility of H atoms in the system.

To further understand these dynamics, the following sections present a detailed trapping model and de-trapping model to quantify the activation energy of trapping and the de-trapping energy barrier. To facilitate the practical quantification of trapping behavior from our MD simulations, we tracked the first-time trapping rate, which measures the frequency of H atoms that initially in the bulk are captured by either the helium bubble or the free surface. By focusing on the initial trapping event, this approach provides a clear and convenient metric for assessing the intrinsic trapping ability of the helium bubble, making the analysis more direct and interpretable.

The de-trapping model was developed by monitoring the decreasing in the number of H atoms at the bubble surface over time. This analysis provides insight into the stability of trapped H atoms and the energy barrier required for their dissociation.

#### 3.3.1. MD-based trapping model

To gain insights into the results of MD simulations, we have introduced a trapping model to quantify the rate at which H atoms migrate from the bulk matrix to sinks such as helium bubbles and the free surface. The trapping process can be treated as a first order parallel reaction [40], expressed as follows:

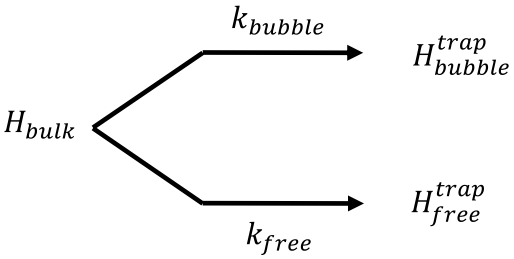


(3)

where $k_{bubble}$and $k_{free}$ are trapping rate constants characterizing the captured efficiency of H atoms by of the bubble and free surface, respectively. Hydrogen interstitials in the Fe matrix follow two distinct pathways, leading to different trapping sites: the helium bubble $H_{bubble}^{trap}$ or the free surface $H_{free}^{trap}$.

The system also follows the conservation of the total number of H atoms:

$$N_{total} = N_{bulk}(t) + N_{bubble}(t) + N_{free}(t), \tag{4}$$

where $N_{bulk}(t)$ is the number of H atoms in the bulk, $N_{bubble}(t)$ is the number of H atoms trapped at the bubble surface, and the $N_{free}(t)$ is the number of H atoms diffused to the free surface, which does not contribute to the He bubble capturing behavior.

The radial distance from the void center, $R_0 = 25.5\ \AA$, marks the peak of hydrogen accumulation and serves as the reference for defining the trapping region, *where H atoms predominantly accumulate, and considers to be trapped by the bubble.* To account for the enhanced vibrational motion of hydrogen atoms on bubble surface at elevated temperatures, the trapping region radius is extended to $R_0 + \delta$, where $\delta$ represents the lattice parameter. Time-averaged hydrogen distributions around the bubble, under various temperatures, are provided in the Supplementary Information S2.

The time evolution of $N_{bulk}(t)$ and $N_{bubble}(t)$, the number of H atoms trapped at the bubble surface, is described by:

$$N_{bulk}(t) = N_{total} * e^{-(k_{bubble}+k_{free})t}, \tag{5}$$

$$N_{bubble}(t) = \frac{k_{bubble}}{k_{bubble}+k_{free}} * N_{total} * \left(1 - e^{-(k_{bubble}+k_{free})t}\right), \tag{6}$$

The time evolution of $N_{bulk}(t)$ and $N_{bubble}(t)$ is illustrated in Figs. 6(a) and (b). Notably, this model focuses on the first-time trapping rate. A decrease to zero of $N_{bulk}(t)$ indicates that every H atom initially in the bulk matrix has already experienced a trapping event, either by the bubble or the free surface. Similarly, when $N_{bubble}(t)$ approaches a constant value, it represents the total number of H atoms that have ever been trapped by the bubble, rather than the number of H atoms currently trapped at a specific time. The detailed derivation process for $N_{bulk}(t)$ and $N_{bubble}(t)$ is provided in the Supplementary information S2.

The time evolution of $N_{bulk}(t)$ and $N_{bubble}(t)$ is illustrated in Figs. 6(a) and (b). Notably, this model focuses on the first-time trapping rate. A decrease to zero of $N_{bulk}(t)$ indicates that every H atom initially in the bulk matrix has already experienced a trapping event, either by the bubble or the free surface. Similarly, when $N_{bubble}(t)$ approaches a constant value, it represents the total number of H atoms that have ever been trapped by the bubble, rather than the number of H atoms currently trapped at a specific time. The trapping rate constant $k_{bubble}$ follows an Arrhenius relationship [40], expressed as:

$$k_{bubble} = \nu \exp\left(-\frac{Q_{trap}^{bubble}}{k_B T}\right) \tag{7}$$

Where $\nu$ is attempt frequency, a temperature-independent term describing the frequency of H atom interactions with the bubble trapping site [41]. $Q_{trap}^{bubble}$, referred to as the trapping enthalpy, represents the average energy barrier that a hydrogen atom in the bulk must overcome to migrate and become trapped at the helium bubble surface. This parameter inherently represents the competition between trapping sites, namely the bubble and the free surface. While the migration and trapping energy barriers for individual H atoms can vary based on their proximity to either trapping site and local conditions, $Q_{trap}^{bubble}$ serves as a system-wide statistical average.

This average accounts for all possible migration pathways, weighted by their likelihood, and reflects the net efficiency of the bubble as a trapping site. The competition is quantified by the rate constants $k_{bubble}$ and $k_{free}$. In the regions where H atoms are closer to the free surface, $k_{free}$ dominates, leading to preferential migration toward the free surface. Conversely, in the regions nearer to the bubble, $k_{bubble}$ governs the trapping behavior.

The parameter $k_{bubble}$ was determined using a non-linear least squares fitting method implemented via the *curve_fit* function from the *scipy.optimize* module in Python [42]. This function applies the Levenberg-Marquardt algorithm to minimize the residual sum of squares between the hydrogen retention data $N_{bubble}(t)$ obtained from MD simulations and the modeled exponential function described in Eq. (6). The

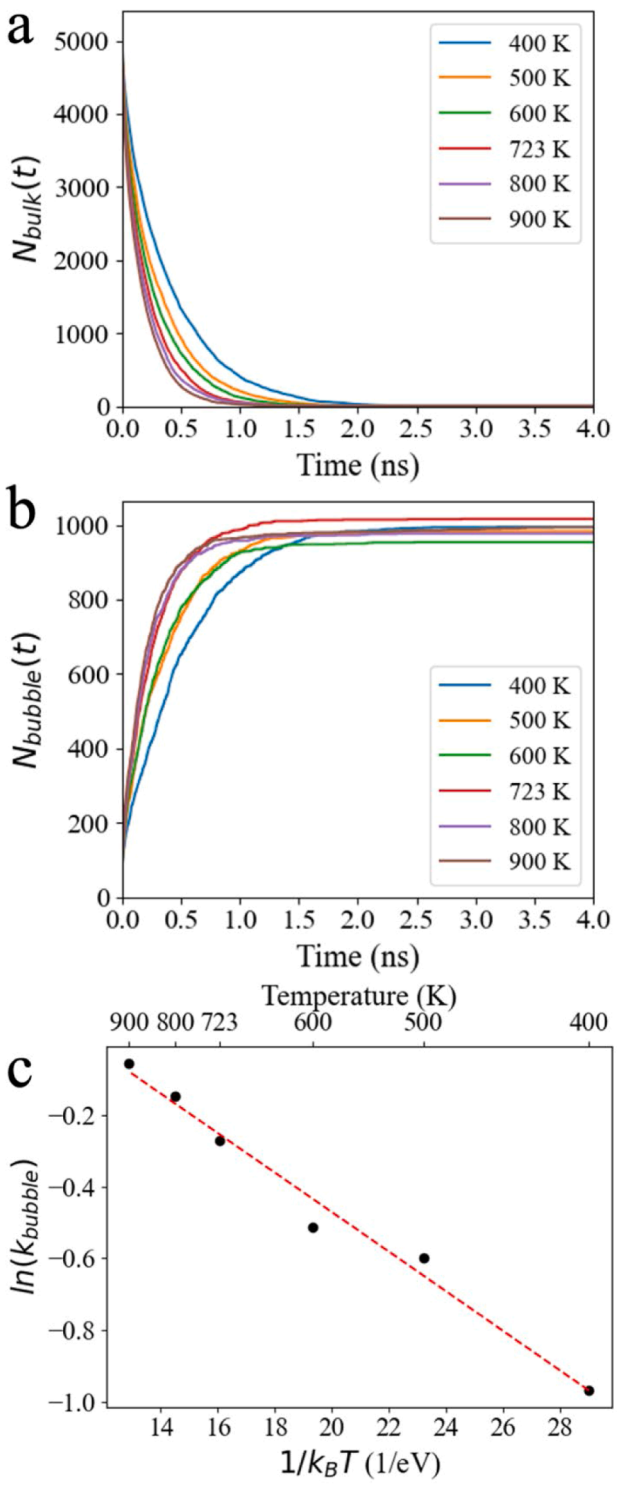


**Fig. 6.** (a) $\boldsymbol{N_{bulk}(t)}$ over time for 400–900 K. $\boldsymbol{N_{bulk}(t)}$ decreases to zero, indicating that all H atoms in the bulk have been trapped either by the bubble or the free surface one time. (b) $\boldsymbol{N_{bubble}(t)}$ stabilizes at a constant value, representing the cumulative number of H atoms trapped by the bubble over time, not the instantaneous trapped count. (c) $\boldsymbol{ln\,(k_{bubble})}$ vs. $\boldsymbol{1/k_BT}$ with a fitted slope of $-0.055 \pm 0.0037$ $\boldsymbol{eV}$.

extracted $k_{bubble}$ values were further analyzed by plotting $\ln(k_{bubble})$ versus $1/k_BT$, as shown in Fig. 6(c). The slope of the resulting linear fit corresponds to $-Q_{trap}^{bubble}$, while the intercept provides the logarithm of the attempt frequency, $\ln(\nu)$. The calculated $Q_{trap}^{bubble}$ is $0.0553 \pm 0.0037$eV which is comparable to the migration energy barrier of H atoms between T sites in bcc Fe, reported to be approximately 0.045 eV [27]. The fitted attempt frequency is 1.91 $ns^{-1}$, reflecting the intrinsic frequency of H atom interactions with the trapping sites at the bubble surface.

### 3.3.2. De-trapping model

The evolution of the number of instantaneous trapped H atoms over time is shown in Fig. 7(a). Initially, the number of trapped H atoms increases as H atoms from the bulk are captured by the helium bubble surface. However, as the system transitions to a state dominated by de-trapping processes, the number of instantaneous trapped H atoms reaches a peak and then begins to decrease. This transition point is highlighted by the vertical dashed lines in Fig. 7(a), which correspond to the maximum number of trapped H atoms at different temperatures. These dashed lines mark the moment when the de-trapping mechanism becomes significant, illustrating the dynamic competition between trapping and de-trapping processes over time. The time corresponding to the peak number of trapped H atoms, $t_{peak}$, is used as a reference point. Beyond $t_{peak}$, the decrease in the number of trapped H atoms follows the exponential decay function:

$$N_{trapped}(t) = N_{peak} e^{-k_{de-trap}\left(t - t_{peak}\right)} \tag{9}$$

Where $N_{peak}$ is the maximum number of trapped H atoms at $t_{peak}$, and $k_{de-trap}$ is the de-trapping rate constant. This rate constant quantifies the probability of H atoms dissociating from the trapping sites over time. Based on the results from MD simulations, the detailed derivation process for $N_{trapped}(t)$ is provided in the Supplementary information S3.

The de-trapping rate constant, $k_{de-trap}$, follows an Arrhenius relationship:

$$k_{de-trap} = \nu' \exp\left(-\frac{Q_{de-trap}}{k_B T}\right) \tag{10}$$

where $\nu'$ is de-trapping attempt frequency, representing the frequency of H atoms attempting to dissociate from the trapping sites, and $Q_{de-trap}$ is energy barrier for de-trapping. The extracted $k_{de-trap}$ values were further analyzed by plotting $\ln(k_{de-trap})$ versus $1/k_BT$, as shown in Fig. 7(b). From the linear fit to the MD results, the slope gives $-Q_{de-trap}$. The calculated $Q_{de-trap}$ is $0.703 \pm 0.038$ $eV$, slightly lower than the single H atom binding energy at the Fe-He interface (0.794 eV), which is likely due to H-H interactions reducing the binding strength [43]. This value is also comparable to the experimental result of 0.75 eV [44]. The de-trapping attempt frequency is ~876 $ns^{-1}$, reflecting the rate at which hydrogen atoms attempt to escape from the bubble surface.

### 3.4. Influence of He/V ratios

The influence of He/V ratios on the trapping and de-trapping behavior of H atoms at 723 K was analyzed across four selected He/V ratios: 0, 0.2, 0.5, and 1. As shown in Fig. 8(a), H atoms exhibit continuous de-trapping from the bubble region over time. With increasing He density, more H atoms are initially trapped. By applying the trapping and de-trapping models, the activation energies $Q_{trap}^{bubble}$ and $Q_{de-trap}$. were calculated and are presented in Fig. 8(b).

With increasing in He/V ratios, $Q_{trap}^{bubble}$ decreases from 0.065 eV at He/V = 0 to 0.049 eV at He/V = 1. This decrease indicates that higher He densities reduce the energy barrier for trapping H atoms, potentially reflecting changes in the local stress and strain fields around the bubble. For $Q_{de-trap}$, the values range from 0.68 eV to 0.70 eV across the He/V ratios, with the largest value observed at He/V = 0.5. The difference between He/V = 0.2 and 0.5 is approximately 0.021 eV, which lies within the propagated uncertainty (≈0.037 eV) of the fitted pre-factor $\ln(\nu') = 6.776 \pm 0.600$. This indicates that the apparent abruptness is not statistically significant, but rather reflects the fitting error, as the

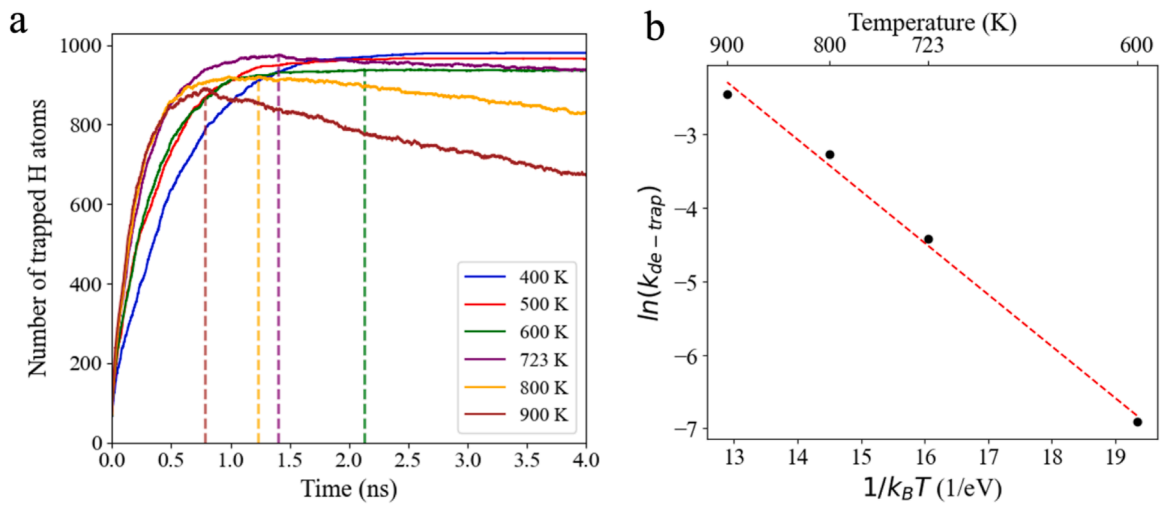


**Fig. 7.** (a) Time evolution of the instantaneous number of H atoms trapped at the bubble surface for a helium bubble with He/V = 0.5. At 600 K and above, a de-trapping process becomes evident, indicated by the peaks in the trapped H atom count and subsequent decline over time. In contrast, at 400 K and 500 K, the number of trapped H atoms stabilizes, with no significant de-trapping observed. The vertical dashed lines highlight the peak trapping points for 600 K, 723 K, 800 K, and 900 K. (b) Plot of $\ln(\boldsymbol{k_{de-trap}})$ versus $1/\boldsymbol{k_BT}$, where the slope represents and the $-\boldsymbol{Q_{de-trap}} = -0.703 \pm 0.038$ $\boldsymbol{eV}$ intercept corresponds to $In(\nu')$.

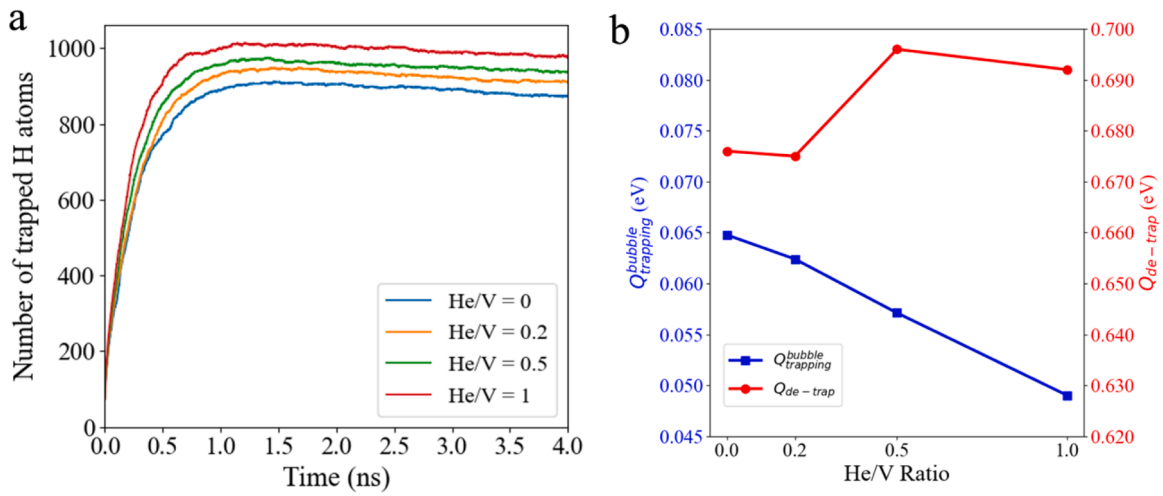


**Fig. 8.** (a) Evolution of trapped H atoms over time at 723 K for helium bubbles at four different He/V ratios (0, 0.2, 0.5, and 1). The number of trapped H atoms represents the instantaneous trapped H atoms at a given time. (b) The activation energies for trapping $\boldsymbol{Q^{bubble}_{trap}}$ and de-trapping $\boldsymbol{Q_{de-trap}}$ as functions of the He/V ratio. $\boldsymbol{Q^{bubble}_{trap}}$ decreases from 0.065 eV at He/V = 0 to 0.049 eV at He/V = 1, demonstrating that higher helium densities reduce the trapping energy barrier, likely due to enhanced stress or strain fields around the bubble. In contrast, $\boldsymbol{Q_{de-trap}}$ remains relatively stable, ranging between 0.68 eV and 0.70 eV, with a peak at He/V = 0.5. This intermediate maximum suggests a stabilization effect in bubble pressure at this ratio, which marginally increases the dissociation barrier.

uncertainty from the de-trapping rate constants themselves is negligible ($\approx 3 \times 10^{-4}$ eV).

In addition, the slight larger $Q_{de-trap}$ at He/V = 0.5 may also be associated with the helium bubble approaching a near-equilibrium pressure state at 723 K, where the stress exerted on the surrounding Fe matrix is minimized [45]. Under such conditions, the reduced interfacial distortion could enhance the hydrogen binding strength, thereby raising the de-trapping barrier. Beyond this state, further increases in helium density would amplify matrix distortion, resulting in lower hydrogen stability.

Overall, the variations in $Q_{de-trap}$ across the He/V ratios remain relatively small, underscoring that the influence of He/V on the de-trapping activation energy is subtle and within statistical uncertainty, without significantly affecting the overall de-trapping dynamics.

To further assess whether hydrogen affects the evolution of helium bubble volumes, we compared the temporal bubble growth at different He/V ratios (0.2, 0.5, and 1.0) with hydrogen present during 2 ns molecular dynamics simulations at 723 K. The results, summarized in Supplementary Fig. S4 and Table S1, indicate that the bubble volumes exhibit the same He/V-dependent trend as in the hydrogen-free case. No significant deviation in either the average bubble volume or its temporal evolution is observed when hydrogen accumulates at the bubble interface. For instance, at He/V = 0.2, the average bubble volume with surface hydrogen is 54.91 ± 1.25 nm$^3$ compared to 54.63 nm$^3$ without hydrogen; at He/V = 1.0, the respective values are 63.14 ± 0.72 nm$^3$ and 63.03 nm$^3$. These findings suggest that, while hydrogen is trapped at helium bubbles, its presence does not substantially alter the bubble volume evolution. Therefore, the dominant factor governing bubble size remains the He/V ratio itself, with hydrogen's role being primarily related to interfacial trapping rather than volumetric growth.

### 3.5. Formation of $H_2$ molecule and H-H interaction

The time-averaged radial pair distribution function (RDF) for H atoms, captured by a He cavity with a He/V = 0.5 at 723 K over a 4 ns simulation, is shown in Fig. 9(a). The RDF displays two prominent peaks. The first peak, located at 0.74 Å, corresponds to the equilibrium bond length of $H_2$ molecules, indicating the formation of $H_2$ within the He cavity. The second peak, at 1.71 $\AA$, represents the preferred nearest-neighbor distance for single H atoms trapped at the Fe-He interface.

To investigate the formation mechanism of $H_2$, we performed CI-NEB calculations on the Fe (010) void surface, as shown in Fig. 9(b). Two separate H atoms initially adsorbed onto the Fe surface (state A) and overcome an energy barrier of 0.90 eV to form an $H_2$ molecule (state B). This energy barrier is consistent with *ab-initio* calculation results [46]. In contrast, the Fe-H interatomic potential developed by Ramasubramaniam et al. [35] results in a significantly higher energy barrier of 3.8 eV, deviating from first-principles calculations. In comparison, the potential we currently used offers a more accurate description, aligning well with DFT predictions and more accurately capturing the thermally activated nature of $H_2$ formation process. Subsequently, the $H_2$ molecule diffuses into the void to state C. This barrier explains the temperature dependence of $H_2$ formation in the system. At 400 K, no $H_2$ is formed inside the He cavity, while at 500 K, only one $H_2$ molecule is observed. By 723 K, 26 $H_2$ molecules form within the He/V = 0.5 bubble. Simulations for He/V = 1 and He/V = 0 bubbles yield 23 and 19 $H_2$ molecules inside the bubble region, respectively, after 4 ns. Within the range of He densities studied, no significant dependence of $H_2$ formation on He density is observed.

The second peak in Fig. 9(a), at 1.71 $\AA$, reflects the preferred nearest-neighbor distance for single H atoms trapped at the Fe-He interface. To explore the origin of this peak, the H-H interaction energy for a H pair located in neighboring sites was evaluated using the binding energy equation:

$$E_B^{H-H} = 2E_{total}^{H} - E_{total}^{2H} - E_{Fe} \tag{11}$$

Here, $E_{total}^{H}$ represents the total energy of a single hydrogen atom at the Fe-He interface, while $E_{total}^{2H}$ is the total energy of two neighboring hydrogen atoms at the interface. $E_{Fe}$ is the energy of the Fe-He supercell without H atoms. A positive $E_B^{H-H}$ indicates an attractive interaction. In this work, the reference energy for a single H atom ($E_{b,\,\hat{y}[010]}^{interface}$) is taken as the binding energy along the $\hat{y}[010]$ direction at the Fe-He interface in the He/V = 0.5 system. The results, shown in Fig. 9(d), reveal that the first nearest-neighbor (1NN) H pair at 1.714 Å exhibits an attractive interaction with a positive $E_B^{H-H}$, explaining the second peak in the RDF. In contrast, the second, third, and fourth nearest-neighbor H pairs exhibit repulsive interactions, while beyond the fifth nearest neighbor, no significant interaction is observed.

Additionally, the binding energy distribution of trapped single H

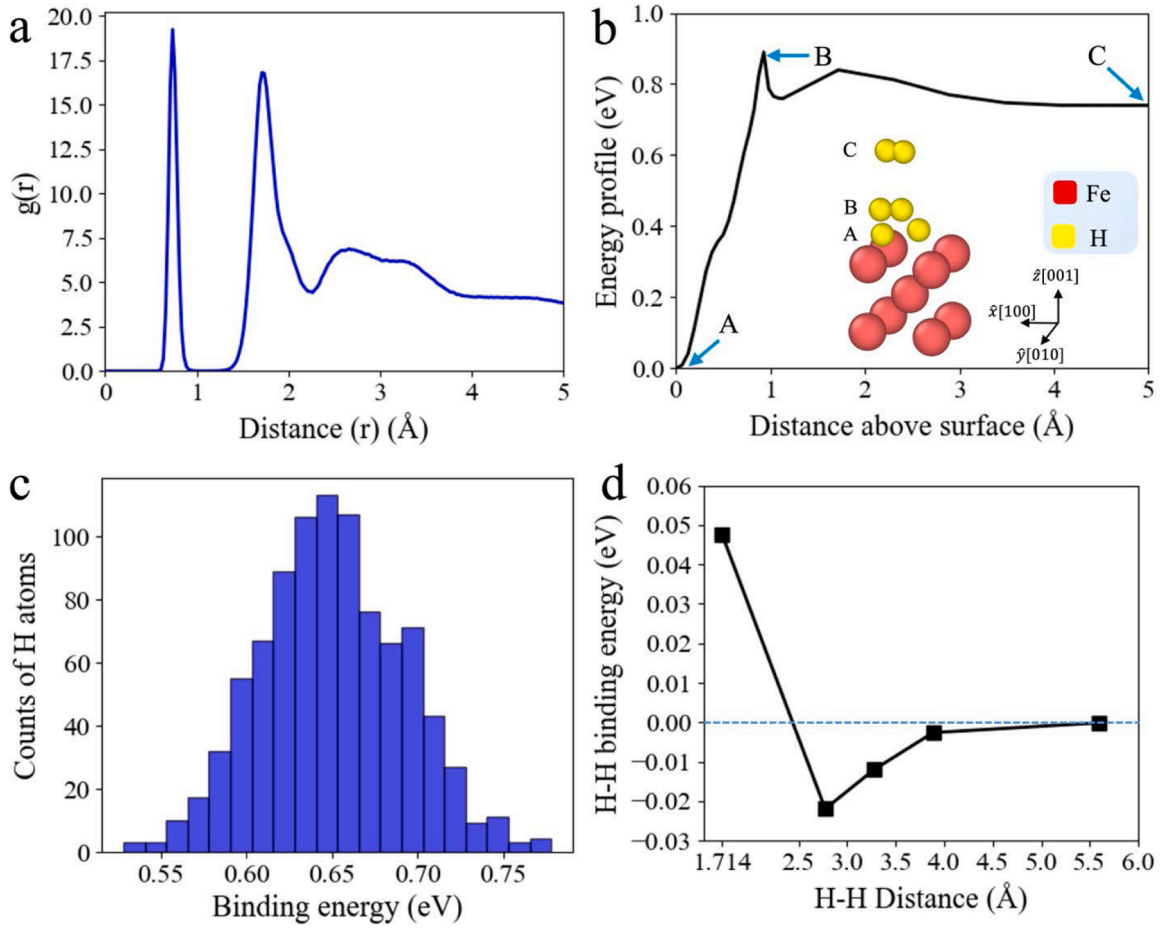


**Fig. 9.** (a) Time-averaged radial pair distribution function for H atoms captured by a He cavity (He/V = 0.5) at 723 K. The first peak at 0.74 Å indicates the equilibrium bond length of $\boldsymbol{H_2}$ molecules, while the second peak at 1.71 Å corresponds to the preferred nearest-neighbor distance for single H atoms trapped at the Fe-He interface. (b) CI-NEB calculation of $\boldsymbol{H_2}$ formation on the Fe (010) void surface. Two H atoms trapped on the surface (state A) overcome an energy barrier of 0.90 eV to form $\boldsymbol{H_2}$ (state B), which then diffuses into the void (state C). (c) Binding energy distribution of single H atoms trapped at the Fe-He interface in the He/V = 0.5 system. The average binding energy is 0.65 eV. (d) H-H binding energy ($\boldsymbol{E_B^{H-H}}$) as a function of the distance between H atoms. An attractive interaction is observed for the first nearest neighbor (1.71 Å).

atoms at the Fe-He interface for the He/V = 0.5 system is shown in Fig. 9 (c). The average binding energy is 0.65 eV, lower than the single H atom binding energy of 0.794 eV. This reduction reflects the influence of multi-H repulsive interactions, which weaken the overall binding of individual H atoms at the interface.

## 4. Conclusion

Molecular static calculations are used to understand the interaction and properties of H at the interface between He bubbles and the BCC Fe matrix. This involves calculating the binding energy of H located along various crystal directions with different He density bubbles and performing CI-NEB calculation of H migration from the interface into the matrix. Across all cavity sizes, the [110] orientation consistently exhibits the highest hydrogen binding energies. An increased helium density (He/V ratio) shifts the preferred binding site due to stress fields. At lower He/V ratios, smaller bubbles have slightly lower binding energies due to higher surface tension, but these differences converge at higher helium densities where the helium-induced stress dominates. The hydrogen migration energy barrier from the Fe–He interface to the Fe bulk strongly depends on helium density and crystallographic direction. Higher helium densities (e.g., He/V = 1.2) destabilize the initial trapping site and flatten the migration path along the $\hat{y}$[010], while the $\hat{y}$[111] orientation remains relatively unaffected, except for minor changes at the highest helium concentration.

Molecular dynamics simulations were performed in a BCC Fe supercell containing a 5 nm void to investigate the capture and release of hydrogen from helium bubbles across temperatures ranging from 400 K to 900 K. A kinetic trapping model was developed to describe the first-time trapping of hydrogen atoms at the bubble surface, following an Arrhenius-type dependence with a trapping activation energy of 0.055 eV—comparable to the known migration barrier of hydrogen in bcc Fe—and an attempt frequency of approximately $1.91\times10^{9}$ $s^{-1}$. Building on this, the de-trapping model tracks the exponential decay of hydrogen bound at the bubble surface over time, yielding a de-trapping activation energy of ~0.703 eV and dissociation temperature in range of 500–600 K. While experiments show that hydrogen remains stable at helium bubble surfaces in RAFM steel F82H at 723 K [12], our simulations indicate otherwise, suggesting the discrepancies that warrant further investigation. An examination of the effects of different helium densities (He/V = 0, 0.2, 0.5, and 1) at 723 K shows that higher He/V ratios lower the trapping energy barrier, indicating that local stress or strain fields created by denser helium bubbles facilitate hydrogen capture. In contrast, the de-trapping activation energy remains relatively stable, with a slight increase at He/V = 0.5, possibly due to the bubble approaching near-equilibrium pressure, which marginally elevates the barrier for H atom dissociation. Overall, these MD simulations highlight the interplay between helium content, temperature, and the trapping/de-trapping dynamics of hydrogen in BCC Fe.

Hydrogen atoms trapped at the Fe–He interface can form $H_2$ molecules with an activation energy of approximately 0.90 eV, or remain as single atoms that interact attractively at a nearest-neighbor distance of 1.71 Å. However, repulsion among multi-H atoms weakens individual binding energies, reducing them from 0.794 eV to an average of 0.65 eV. This highlights the complex interplay of molecular formation and H–H interactions at the interface. These findings provide insights into the retention and trapping behavior of hydrogen at helium bubbles in iron-based materials, informing strategies to mitigate tritium sequestration and material degradation in fusion reactor components.

## CRediT authorship contribution statement

**Lihao Shi:** Writing – review & editing, Writing – original draft, Visualization, Validation, Methodology, Investigation, Formal analysis, Data curation, Conceptualization. **Cianna Chen:** Formal analysis, Investigation, Visualization, Writing – review & editing. **Qing Peng:** Writing – review & editing, Supervision, Resources, Methodology, Conceptualization. **Fei Gao:** Writing – review & editing, Supervision, Resources, Methodology, Conceptualization.

## Declaration of competing interest

The authors declare that they have no known competing financial interests or personal relationships that could have appeared to influence the work reported in this paper.

## Acknowledgements

This work was supported by the U.S. Department of Energy, Office of Science, Office of Fusion Energy Sciences under Award Number DE-SC0020226.

## Supplementary materials

Supplementary material associated with this article can be found, in the online version, at doi:10.1016/j.jnucmat.2025.156171.

## Data availability

Data will be made available on request.

## References

[1] S.J. Zinkle, J.T. Busby, Structural materials for fission & fusion energy, Mater. Today 12 (2009) 12–19, https://doi.org/10.1016/S1369-7021(09)70294-9.
[2] J.H. Evans, Irradiation-induced cavity lattice formation in metals, Patterns Defects Mater. Instab. (1990) 347–370, https://doi.org/10.1007/978-94-009-0593-1_23.
[3] K. Farrell, Experimental effects of helium on cavity formation during irradiation—A review, Radiat. Eff. 53 (1980) 175–194, https://doi.org/10.1080/00337578008207114.
[4] H. Zhang, Z. Yao, M.R. Daymond, M.A. Kirk, Cavity morphology in a Ni based superalloy under heavy ion irradiation with cold pre-injected helium. I, J. Appl. Phys. 115 (2014), https://doi.org/10.1063/1.4867637.
[5] W. Han, E.G. Fu, M.J. Demkowicz, Y. Wang, A. Misra, Irradiation damage of single crystal, coarse-grained, and nanograined copper under helium bombardment at 450 °C, J. Mater. Res. 28 (2013) 2763–2770, https://doi.org/10.1557/jmr.2013.283.
[6] L. Yang, F. Gao, R.J. Kurtz, X.T. Zu, Atomistic simulations of helium clustering and grain boundary reconstruction in alpha-iron, Acta Mater. 82 (2015) 275–286, https://doi.org/10.1016/j.actamat.2014.09.015.
[7] L. Yang, F. Gao, R.J. Kurtz, X.T. Zu, S.M. Peng, X.G. Long, X.S. Zhou, Effects of local structure on helium bubble growth in bulk and at grain boundaries of bcc iron: A molecular dynamics study, Acta Mater. 97 (2015) 86–93, https://doi.org/10.1016/j.actamat.2015.06.055.
[8] K. Farrell, E. Lee, Ion damage in a Fe-10Cr-6Mo-0.5Nb ferritic steel, in: Radiat.-Induc. Chang. Microstruct. 13th Int. Symp. Part I, ASTM International100 Barr Harbor Drive, PO Box C700, West Conshohocken, PA 19428-2959, 1987: pp. 498–507. https://doi.org/10.1520/STP33839S.
[9] E. Wakai, T. Sawai, K. Furuya, A. Naito, T. Aruga, K. Kikuchi, S. Yamashita, S. Ohnuki, S. Yamamoto, H. Naramoto, S. Jistukawa, Effect of triple ion beams in ferritic/martensitic steel on swelling behavior, J. Nucl. Mater. 307-311 (2002) 278–282, https://doi.org/10.1016/S0022-3115(02)01076-0.
[10] E. Wakai, K. Kikuchi, S. Yamamoto, T. Aruga, M. Ando, H. Tanigawa, T. Taguchi, T. Sawai, K. Oka, S. Ohnuki, Swelling behavior of F82H steel irradiated by triple/dual ion beams, J. Nucl. Mater. 318 (2003) 267–273.
[11] W. Hu, L. Guo, J. Chen, F. Luo, T. Li, Y. Ren, J. Suo, F. Yang, Synergistic effect of helium and hydrogen for bubble swelling in reduced-activation ferritic/martensitic steel under sequential helium and hydrogen irradiation at different temperatures, Fusion Eng. Des. 89 (2014) 324–328, https://doi.org/10.1016/j.fusengdes.2014.02.033.
[12] L.N. Clowers, Z. Jiao, G.S. Was, Synergies between H, He and radiation damage in dual and triple ion irradiation of candidate fusion blanket materials, J. Nucl. Mater. 565 (2022) 153722, https://doi.org/10.1016/j.jnucmat.2022.153722.
[13] C. Judge, H. Rajakumar, A. Korinek, G. Bickel, On the potential synergies of helium and hydrogen on the nucleation and stability of cavity clusters in Inconel X-750® irradiated in a high thermal neutron flux spectra, in: 2019.
[14] N. Zimber, P. Vladimirov, M. Klimenkov, U. Jäntsch, R. Vila, V. Chakin, F. Mota, Microstructural evolution of three potential fusion candidate steels under ion-irradiation, J. Nucl. Mater. 535 (2020) 152160, https://doi.org/10.1016/j.jnucmat.2020.152160.
[15] W.A. Counts, C. Wolverton, R. Gibala, First-principles energetics of hydrogen traps in α-Fe: point defects, Acta Mater 58 (2010) 4730–4741, https://doi.org/10.1016/j.actamat.2010.05.010.

[16] J. Marian, T. Hoang, M. Fluss, L.L. Hsiung, A review of helium–hydrogen synergistic effects in radiation damage observed in fusion energy steels and an interaction model to guide future understanding, J. Nucl. Mater. 462 (2015) 409–421, https://doi.org/10.1016/j.jnucmat.2014.12.046.
[17] E. Hayward, C. Deo, Synergistic effects in hydrogen–helium bubbles, J. Phys. Condens. Matter 24 (2012) 265402, https://doi.org/10.1088/0953-8984/24/26/265402.
[18] C.J. Ortiz, R. Vila, J.M. Pruneda, Ab initio study of helium and hydrogen interactions in $\alpha$-Fe. http://arxiv.org/abs/1205.6374, 2012 (accessed April 8, 2024).
[19] Z.J. Bergstrom, L. Yang, B.D. Wirth, Hydrogen trapping energetics at BCC iron-helium interfaces, J. Nucl. Mater. 572 (2022) 154064, https://doi.org/10.1016/j.jnucmat.2022.154064.
[20] Z. Chen, L. Yang, X. Hu, B.D. Wirth, M. Ye, MD simulation of the He bubble effect on H retention in BCC iron, Fusion Eng. Des. 180 (2022) 113184, https://doi.org/10.1016/j.fusengdes.2022.113184.
[21] J. Song, W.A. Curtin, Atomic mechanism and prediction of hydrogen embrittlement in iron, Nat. Mater. 12 (2013) 145–151, https://doi.org/10.1038/nmat3479.
[22] F. Wu, Z. Liu, Y. Chen, X. Guo, J. Xue, Y. Li, H. Huang, H. Zhou, H. Deng, Deep learning-based neural network potential for investigating the synergistic effect of H and He in BCC-Fe, Comput. Mater. Sci. 246 (2025) 113434, https://doi.org/10.1016/j.commatsci.2024.113434.
[23] S. Plimpton, Fast parallel algorithms for short-range molecular dynamics, J. Comput. Phys. 117 (1995) 1–19, https://doi.org/10.1006/jcph.1995.1039.
[24] F. Gao, H. Deng, H.L. Heinisch, R.J. Kurtz, A new Fe–He interatomic potential based on ab initio calculations in α-Fe, J. Nucl. Mater. 418 (2011) 115–120, https://doi.org/10.1016/j.jnucmat.2011.06.008.
[25] G.J. Ackland, M.I. Mendelev, D.J. Srolovitz, S. Han, A.V. Barashev, Development of an interatomic potential for phosphorus impurities in -iron, J. Phys. Condens. Matter 16 (2004) S2629–S2642, https://doi.org/10.1088/0953-8984/16/27/003.
[26] R.A. Aziz, A.R. Janzen, M.R. Moldover, Ab initio calculations for helium: A standard for transport property measurements, Phys. Rev. Lett. 74 (1995) 1586–1589, https://doi.org/10.1103/PhysRevLett.74.1586.
[27] M. Wen, A new interatomic potential describing Fe-H and H-H interactions in bcc iron, Comput. Mater. Sci. 197 (2021) 110640, https://doi.org/10.1016/j.commatsci.2021.110640.
[28] D.K. Belashchenko, The simulation of metallic hydrogen-helium solutions under the conditions of internal Jupiter regions, Russ. J. Phys. Chem. 80 (2006) S31–S39, https://doi.org/10.1134/S0036024406130061.
[29] A. Stukowski, Visualization and analysis of atomistic simulation data with OVITO–the open visualization tool, Model. Simul. Mater. Sci. Eng. 18 (2010) 015012, https://doi.org/10.1088/0965-0393/18/1/015012.
[30] G. Henkelman, B.P. Uberuaga, H. Jónsson, A climbing image nudged elastic band method for finding saddle points and minimum energy paths, J. Chem. Phys. 113 (2000) 9901–9904, https://doi.org/10.1063/1.1329672.
[31] G. Henkelman, H. Jónsson, Improved tangent estimate in the nudged elastic band method for finding minimum energy paths and saddle points, J. Chem. Phys. 113 (2000) 9978–9985, https://doi.org/10.1063/1.1323224.
[32] S. Nosé, A molecular dynamics method for simulations in the canonical ensemble, Mol. Phys. 100 (2002) 191–198, https://doi.org/10.1080/00268970110089108.
[33] W.G. Hoover, Canonical dynamics: equilibrium phase-space distributions, Phys. Rev. A 31 (1985) 1695–1697, https://doi.org/10.1103/PhysRevA.31.1695.
[34] D.E. Jiang, E.A. Carter, Diffusion of interstitial hydrogen into and through bcc Fe from first principles, Phys. Rev. B 70 (2004) 064102, https://doi.org/10.1103/PhysRevB.70.064102.
[35] A. Ramasubramaniam, M. Itakura, E.A. Carter, Interatomic potentials for hydrogen in α –iron based on density functional theory, Phys. Rev. B 79 (2009) 174101, https://doi.org/10.1103/PhysRevB.79.174101.
[36] H.-B. Zhou, S. Jin, Y. Zhang, G.-H. Lu, F. Liu, Anisotropic strain enhanced hydrogen solubility in bcc metals: the independence on the sign of strain, Phys. Rev. Lett. 109 (2012) 135502, https://doi.org/10.1103/PhysRevLett.109.135502.
[37] C.-F. Huo, Y.-W. Li, J. Wang, H. Jiao, Surface structure and energetics of hydrogen adsorption on the Fe(111) Surface, J. Phys. Chem. B 109 (2005) 14160–14167, https://doi.org/10.1021/jp051907s.
[38] J. Li, Atomistic local strain. [Online]. Available: http://li.mit.edu/A/Graphics/A/Doc/vonMisesInvariant.pdf. [Accessed: Sep. 20, 2025].
[39] J. Li, F. Shimizu, Least-square atomic strain, 2005, [Online]. Available: http://li.mit.edu/A/Graphics/A/annotate_atomic_strain/Doc/main.pdf.
[40] S.K. Upadhyay, Chemical Kinetics and Reaction Dynamics, Springer Anamaya, New York New Delhi, 2006.
[41] G.S. Was, Fundamentals of Radiation Materials Science, Springer New York, New York, NY, 2017, https://doi.org/10.1007/978-1-4939-3438-6.
[42] P. Virtanen, R. Gommers, T.E. Oliphant, M. Haberland, T. Reddy, D. Cournapeau, E. Burovski, P. Peterson, W. Weckesser, J. Bright, S.J. Van Der Walt, M. Brett, J. Wilson, K.J. Millman, N. Mayorov, A.R.J. Nelson, E. Jones, R. Kern, E. Larson, C. J. Carey, İ. Polat, Y. Feng, E.W. Moore, J. VanderPlas, D. Laxalde, J. Perktold, R. Cimrman, I. Henriksen, E.A. Quintero, C.R. Harris, A.M. Archibald, A.H. Ribeiro, F. Pedregosa, P. Van Mulbregt, , SciPy 1.0 Contributors, A. Vijaykumar, A. P. Bardelli, A. Rothberg, A. Hilboll, A. Kloeckner, A. Scopatz, A. Lee, A. Rokem, C. N. Woods, C. Fulton, C. Masson, C. Häggström, C. Fitzgerald, D.A. Nicholson, D. R. Hagen, D.V. Pasechnik, E. Olivetti, E. Martin, E. Wieser, F. Silva, F. Lenders, F. Wilhelm, G. Young, G.A. Price, G.-L. Ingold, G.E. Allen, G.R. Lee, H. Audren, I. Probst, J.P. Dietrich, J. Silterra, J.T. Webber, J. Slavič, J. Nothman, J. Buchner, J. Kulick, J.L. Schönberger, J.V. De Miranda Cardoso, J. Reimer, J. Harrington, J.L. C. Rodríguez, J. Nunez-Iglesias, J. Kuczynski, K. Tritz, M. Thoma, M. Newville, M. Kümmerer, M. Bolingbroke, M. Tartre, M. Pak, N.J. Smith, N. Nowaczyk, N. Shebanov, O. Pavlyk, P.A. Brodtkorb, P. Lee, R.T. McGibbon, R. Feldbauer, S. Lewis, S. Tygier, S. Sievert, S. Vigna, S. Peterson, S. More, T. Pudlik, T. Oshima, T.J. Pingel, T.P. Robitaille, T. Spura, T.R. Jones, T. Cera, T. Leslie, T. Zito, T. Krauss, U. Upadhyay, Y.O. Halchenko, Y. Vázquez-Baeza, SciPy 1.0: fundamental algorithms for scientific computing in Python, Nat. Methods 17 (2020) 261–272, https://doi.org/10.1038/s41592-019-0686-2.
[43] Y. Cui, C. Hu, P. Yu, D. Xie, L. Kong, Y. Rong, M. Wen, J. Zou, Enhanced H-H binding and consequent H-aggregation around dislocation in α-Fe lattice, Mater. Res. Express 7 (2020) 066518. https://doi.org/10.1088/2053-1591/ab9a81.
[44] S.M. Myers, F. Besenbacher, Deuterium in He-implanted Fe: trapping and the surface permeation barrier, Appl. Phys. Lett. 39 (1981) 450–452.
[45] R.E. Stoller, Yu.N. Osetsky, An atomistic assessment of helium behavior in iron, J. Nucl. Mater. 455 (2014) 258–262, https://doi.org/10.1016/j.jnucmat.2014.06.020.
[46] A. Boda, S.M. Ali, First principles DFT analysis on the diffusion kinetics of hydrogen isotopes through bcc iron (Fe): role of temperature and surface coverage, Int. J. Hydrog. Energy 47 (2022) 31481–31498, https://doi.org/10.1016/j.ijhydene.2022.07.055.